ADVANCED FUNCTIONAL MATERIALS
www.afm-journal.de

Materials Views
www.MaterialsViews.com

Binary $Li_4Ti_5O_{12}$-$Li_2Ti_3O_7$ Nanocomposite as an Anode Material for Li-Ion Batteries

*Guan-Nan Zhu, Long Chen, Yong-Gang Wang, Con-Xiao Wang, Ren-Chao Che, and Yong-Yao Xia**

$Li_4Ti_5O_{12}$ typically shows a flat charge/discharge curve, which usually leads to difficulty in the voltage-based state of charge (SOC) estimation. In this study, a facile quench-assisted solid-state method is used to prepare a highly crystalline binary $Li_4Ti_5O_{12}$-$Li_2Ti_3O_7$ nanocomposite. While $Li_4Ti_5O_{12}$ exhibits a sudden voltage rise/drop near the end of its charge/discharge curve, this binary nanocomposite has a tunable sloped voltage profile. The nanocomposite exhibits a unique lamellar morphology consisting of interconnected nanograins of ≈20 nm size with a hierarchical nanoporous structure, contributing to an enhanced rate capability with a capacity of 128 mA h g^{-1} at a high C-rate of 10 C, and excellent cycling stability.

1. Introduction

Li-ion batteries have been widely used in portable electronics, and their potential applications in electric vehicles (EV, hybrid EV (HEV), plug-in hybrid EV (PHEV)) and stationary energy storage have also been demonstrated.[1–3] As an alternative to traditional carbonaceous materials for anodes, the spinel $Li_4Ti_5O_{12}$ has been extensively studied for its use in Li-ion batteries because it exhibits excellent Li-ion insertion/extraction reversibility with zero structural change and a relatively higher operating voltage (1.55 V vs Li/Li^+), which ensure additional safety by avoiding lithium dendrites.[4,5] Despite the evident advantages, the rate capability of $Li_4Ti_5O_{12}$ is relatively low because of its poor electronic conductivity ($<10^{-13}$ S cm^{-1}) and sluggish lithium-ion diffusion.[6–8] To date, many research efforts have been focused on overcoming these drawbacks in two typical ways. One way aims to enhance the electronic conductivity by doping the spinel with metal or nonmetal ions or by surface modification using conductive coating species.[9–12] The other way is to shorten the diffusion lengths of the Li ions by preparing nanostructured materials with various morphologies.[13–16]

In addition to the important issue of energy and power densities, in order to take full advantage of Li-ion batteries in practical use, a key safety-related issue is efficient energy management using the real-time prediction of the SOC (state of charge); this is especially important for the large batteries in EV applications.[17,18] The voltage-based SOC estimation, typically based on a predetermined OCV–SOC relationship (OCV: open-circuit voltage), is highly challenging in cells with electrodes exhibiting a flat charge/discharge plateau because the voltage profile of the cell remains substantially flat over a broad SOC range but an abrupt voltage rise/drop takes place near the end of the charge/discharge process; as a result, any small errors in the OCV prediction could cause large deviations in the SOC estimation, further contributing to the overcharging/overdischarging problem.[19–21] $Li_4Ti_5O_{12}$ typically shows a very flat voltage profile followed by an abrupt rise/drop near the end of charge/discharge process, and this feature leads to great difficulty in the SOC estimation when it is combined with a cathode material exhibiting a similar charge/discharge behavior. A typical example is the $Li_4Ti_5O_{12}/LiFePO_4$ battery system: it delivers approximately 90% capacity in a very flat plateau, which ensures a smooth voltage output over a wide SOC range, but subsequently, it exhibits a sudden voltage rise/drop at the end of charge/discharge process, which poses a great threat to the voltage-based SOC estimation and consequently the safety of the whole battery system.[22,23] Therefore, it is quite important but challenging to modify the shape of charge/discharge curve of the $Li_4Ti_5O_{12}$ anode. However, very few studies have been focused in this direction.

In the present study, we introduce a facile way to prepare the highly crystalline binary $Li_4Ti_5O_{12}$-$Li_2Ti_3O_7$ nanocomposite, which exhibits a significantly improved voltage profile shape near the end of its charge/discharge process. The effects of the preparation conditions on its phase composition, morphology and electrochemical performance are extensively studied. Also, the successful voltage-based SOC estimation for a $Li_4Ti_5O_{12}/LiFePO_4$ full cell are elucidated.

2. Results and Discussion

It has been demonstrated that Li-ion intercalation can also occur reversibly in the ramsdellite-type structure $Li_2Ti_3O_7$.

G.-N. Zhu, L. Chen, Y.-G. Wang, C.-X. Wang, Prof. Y.-Y. Xia
Department of Chemistry and Shanghai Key Laboratory of Molecular Catalysis and Innovative Materials
Institute of New Energy
Fudan University, Shanghai 200438, China
E-mail: yyxia@fudan.edu.cn
Prof. R.-C. Che
Department of Materials Science and Advanced Materials Laboratory
Fudan University
Shanghai 200438, China

DOI: 10.1002/adfm.201201741

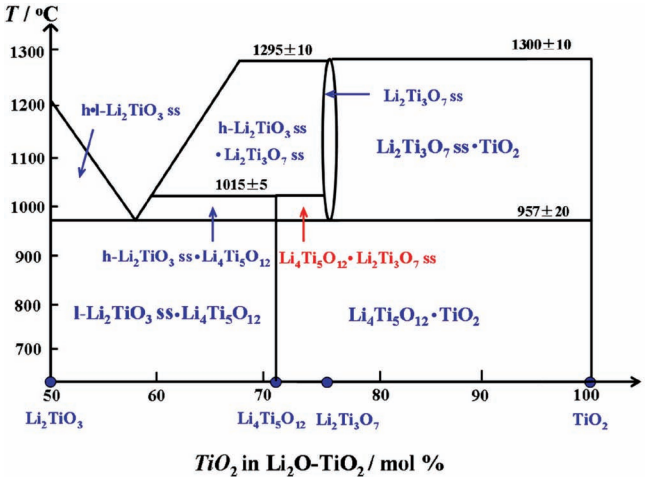

Figure 1. The partial phase diagram of lithium titanates.The 'h', 'l' and 'ss' represent 'high', 'low' and 'solid solution', respectively. Reproduced with permission.[28] Copyright 2009, Elsevier.

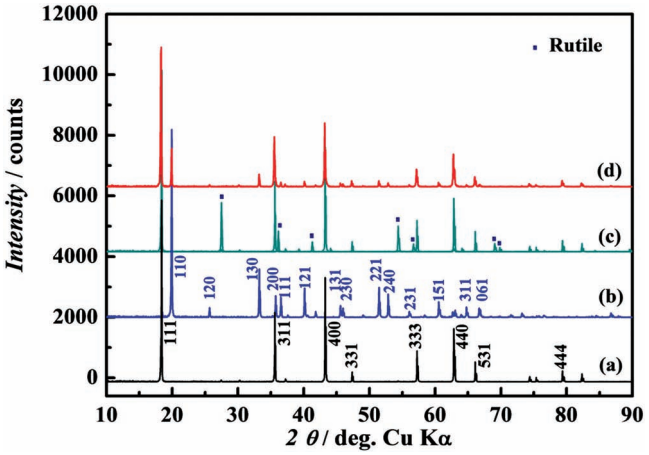

Figure 2. The XRD patterns of single-phase $Li_4Ti_5O_{12}$ (a), single-phase $Li_2Ti_3O_7$ (b), and the LTO-NC (c) and LTO-Q (d) samples. The specific sample in (d) corresponds to LTO-Q-2.

Theoretically, 2.28 lithium ions can be electrochemically intercalated into $Li_2Ti_3O_7$ to give a specific capacity of 235 mA h g^{-1}. Contrary to the reaction mechanism of two-phase co-existence for $Li_4Ti_5O_{12}$, the intercalation/extraction of $Li_2Ti_3O_7$ proceeds in a solid-solution manner or one-phase intercalation mechanism by adopting a single sloping curve in the voltage range of 2.1–1.3 V, accompanied by a small volume change of approximately 2%.[24–27] To achieve the full requirement of $Li_4Ti_5O_{12}$ with high rate capability, long cycling stability, and a sloping curve at the end of charge/discharge process, we designed a nanocomposite by incorporating the $Li_2Ti_3O_7$ phase into $Li_4Ti_5O_{12}$. **Figure 1** shows the phase diagram of lithium titanates, showing how different temperature ranges correspond to different phases. The single-phase formation of $Li_4Ti_5O_{12}$ occurs at <1015±5°C and that of $Li_2Ti_3O_7$ at >957±20°C, while the two phases only co-exist at a narrow range between 957(±20) and 1015(±5)°C, and the coexisting $Li_4Ti_5O_{12}$-$Li_2Ti_3O_7$ dual-phase can be easily transformed into a mixture of $Li_4Ti_5O_{12}$ and TiO_2 by slow cooling.[28,29] Therefore, in the present work, a N_2-quenching method was applied to "freeze" the phase structure formed within the narrow temperature range in order to get the $Li_4Ti_5O_{12}$-$Li_2Ti_3O_7$ dual-phase sample. Experiments were performed at the annealing temperature of 970 °C for 14 h, followed by quench in N_2 (forming the quenched sample, LTO-Q), or by natural cooling (the LTO-NC sample). **Figure 2** gives the X-ray diffraction (XRD) patterns of single-phase $Li_4Ti_5O_{12}$, single-phase $Li_2Ti_3O_7$, and LTO-Q and LTO-NC samples. It is obvious that the LTO-Q sample consists of two phases (Figure 2): the diffraction peaks at 18.4, 30.2, 35.6, 37.1, 43.3, 47.4, 57.2, 62.8, 66.1, 74.3, 75.4, 79.4, and 82.3° (2θ) could be indexed to the cubic spinel phase, $Li_4Ti_5O_{12}$ (space group $Fd\bar{3}m$ (#227), Joint Committee on Powder Diffraction Standards (JCPDS) No. 49-0207),0 while other peaks at 19.9, 33.3, 35.8, 36.5, 40.2, 45.7, 46.1, 51.5, 52.9, 60.6 and 64.8° (2θ) are consistent with the orthorhombic ramsdellite-type, $Li_2Ti_3O_7$ (space group *Pbnm* (#62), JCPDS No. 34-0393), and no other phase formation was detected. By contrast, the LTO-NC sample is identified to comprise $Li_4Ti_5O_{12}$ and rutile TiO_2 (Figure 2c). Furthermore, by employing the same quench-assisted solid-state process, a series of LTO-Q samples with different ratios of $Li_4Ti_5O_{12}$:$Li_2Ti_3O_7$ were synthesized. The XRD patterns of this series are shown in **Figure 3**, and all the samples show very similar diffraction lines, but with a slight difference in the line intensity. As confirmed by transmission electron microscopy (TEM, shown later), the LTO-Q samples contain a highly crystalline phase with no amorphous phase being detected, even in an expanded area as large as 100 nm. Therefore, the phase compositions of the LTO-Q series can be determined using the XRD analysis. Here, Rietveld refinement was conducted under a two-phase analysis mode (**Figure 4**), and the results are summarized in **Table 1**. The phase compositions of the $Li_4Ti_5O_{12}$-$Li_2Ti_3O_7$ samples are determined to be 86.6(1):13.3(9) (LTO-Q-1), 75.2(5):24.7(5) (LTO-Q-2), and 65.4(6):34.5(4) (LTO-Q-3), with low weighted-profile residual factors, R_{wp}, 2 indicating a good agreement between experiment and simulation. The analytical results are very close to weight ratios of the targeted $Li_4Ti_5O_{12}$-$Li_2Ti_3O_7$, also verifying the phase purity of all the LTO-Q samples.

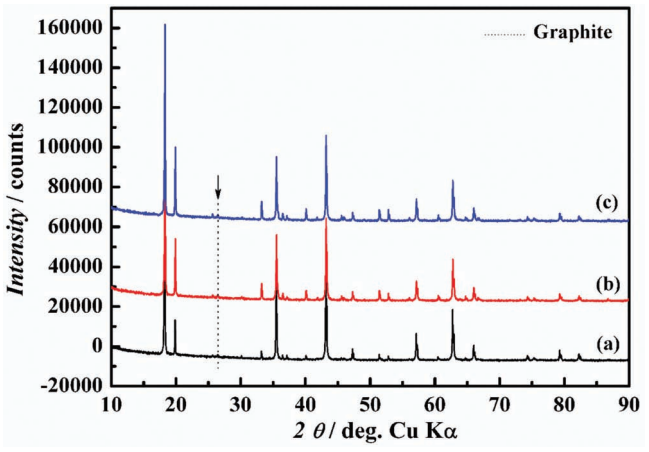

Figure 3. The XRD patterns of the LTO-Q-1 (a), LTO-Q-2 (b), and LTO-Q-3 (c) samples, using graphite for calibration.

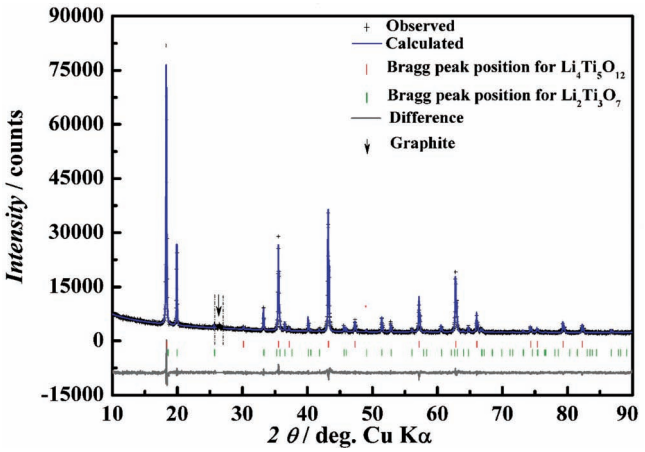

Figure 4. The Rietveld refinement plots of the XRD pattern for the LTO-Q-2 sample.

The morphology and microstructure of LTO-Q (represented by LTO-Q-2) and LTO-M, a lithium titanate mixture produced by mechanically mixing single-phase $Li_4Ti_5O_{12}$ and $Li_2Ti_3O_7$,4 were analyzed by scanning electron microscopy (SEM) and TEM. Comparing the SEM images in **Figure 5**A and D, we find that both samples show a loose accumulation of sub-micrometer particles with a similar diameter of about 120 nm, as a result of high-energy ball milling. However, the TEM images reveal a significant difference in the microstructures of LTO-Q and LTO-M. For LTO-Q, as shown in Figure 5B, each single sub-micrometer particle is a nanocluster, and it is further identified to be composed of smaller nanograins of about 20 nm (Figure 5C), which are interconnected to present a lamellar morphology accumulating in thin layers. In the case of LTO-M, as revealed by Figure 5E and F, only a distribution of dense particles was found; nanograins do not exist in the interior, suggesting a strikingly different result between the conventional and quench-assisted solid-state processes. Additionally, due to the agglomeration of nanograins, the LTO-Q sample shows a nanoporous character, which is confirmed by N_2 adsorption–desorption isotherms (**Figure 6**A) and the corresponding Barrett–Joyner–Halenda (BJH) pore size distribution (Figure 6B). The pore size distribution is not uniform, but it exhibits a hierarchical feature. A relatively broad pore size distribution ranging from 3 to 5 nm corresponds to an accumulation of the ≈20 nm nanograins and/or thin layers, which serves as a natural consequence of the quenching in N_2. More specifically, owing to a tremendous temperature gap, the crystallographic structure of LTO-Q cracks in an instant to produce numerous crystalline layers and nanograins, which contribute to the nanopores. Meanwhile, a narrow peak appears in the size distribution at the pore size of 12 nm, which corresponds to the stacking of the sub-micrometer particles (≈120 nm). It could be assumed that the mesopores of 12 nm and of 3–5 nm could form the main and branch transport paths to facilitate the fast penetration of electrolyte deep into the electrode interior, which is essential for the high rate performance.[14,30,31] Also, based on the N_2 sorption isotherms, the surface area of LTO-Q was determined to be 21.5 m^2 g^{-1} calculated by the Brunauer–Emmett–Teller (BET) method.

Table 1. A comparison of the phase composition of $Li_4Ti_5O_{12}$-$Li_2Ti_3O_7$ based on the targeted values and the Rietveld refinement results of the XRD patterns for the LTO-Q-1, LTO-Q-2, and LTO-Q-3 samples.

Samples	Targeted phase composition of $Li_4Ti_5O_{12}$-$Li_2Ti_3O_7$ [wt%:wt%]	Refined phase composition of $Li_4Ti_5O_{12}$-$Li_2Ti_3O_7$ [wt%:wt%]	R_{wp} [%]
LTO-Q-1	85:15	86.6(1):13.3(9)	5.62(4)
LTO-Q-1	75:25	75.2(5):24.7(5)	5.31(1)
LTO-Q-3	65:35	65.4(6):34.5(4)	4.76(5)

Furthermore, the high-resolution (HR) TEM images in **Figure 7** provide clear microstructure details for the nanograins. The clear lattice fringes in Figure 7A demonstrate the high crystallinity of the LTO-Q sample, which is consistent with the sharp reflections in the XRD (Figure 3 and 4). Upon observation at higher magnification, the nanograins are revealed to comprise two types of interconnected nanocrystals with distinctive crystallographic plane structures, giving important clues to the dual-phase formation (Figure 7B). Two sets of intersecting lattice fringes in region I and II are indexed and calibrated to have a lattice spacing of d = 3.4 and 4.8 Å, 5corresponding to the (120) plane of $Li_2Ti_3O_7$ and (111) plane of $Li_4Ti_5O_{12}$, respectively. Meanwhile, the corresponding fast Fourier transformation (FFT) images show glowing bright spots arranged in two different symmetrical patterns; regions I and II belong to the orthorhombic structure of $Li_2Ti_3O_7$ and the cubic structure of $Li_4Ti_5O_{12}$, respectively. Both results confirm that the two phases of $Li_4Ti_5O_{12}$ and $Li_2Ti_3O_7$ co-exist at the nanoscale regime within 20-nm-sized nanograins; thus, the LTO-Q sample can be referred as a nanocomposite, which is much different from the LTO-M sample, which is a simple mechanical mixture of $Li_4Ti_5O_{12}$ and $Li_2Ti_3O_7$. However, contrary to the clear interfacial boundaries observed in the formation of amorphous domains for composite samples in some studies,[32] the transitional areas between the two phases in LTO-Q are difficult to detect. This may be interpreted in terms of the distribution of the highly crystalline $Li_4Ti_5O_{12}$-$Li_2Ti_3O_7$ dual phase over the entire area of LTO-Q sample.

The electrochemical behavior of the LTO-Q series were systematically investigated and compared with that of single-phase $Li_4Ti_5O_{12}$ and $Li_2Ti_3O_7$ as well as that of LTO-M. **Figure 8**A shows the charge/discharge curves at a C-rate of 0.2 C between 1.0 and 3.0 V. The single-phase $Li_2Ti_3O_7$ sample exhibits a single sloping charge/discharge curve in the voltage range of 2.1–1.3 V and gives a specific capacity of 175 mA h g^{-1}; while the single-phase $Li_4Ti_5O_{12}$ sample delivers a capacity of 160 mA h g^{-1} in a typical charge/discharge curve, in which the potential rapidly drops from 2.6 V to reach a well-defined flat plateau at around 1.55 V (vs Li/Li^+), followed by an abrupt voltage rise/drop near the end of charge/discharge process. Combining the characteristics of the two single phases, the LTO-Q-2 sample delivers a capacity of 165 mA h g^{-1} via a two prolonged sloped voltage profiles before and after the flat plateau at 1.55 V (vs Li/Li^+), inheriting the single-phase regime from the $Li_2Ti_3O_7$ phase while preserving the bi-phasic area typical of the $Li_4Ti_5O_{12}$ phase; such features are more clearly revealed in the plot of voltage as a function of SOC in Figure 8B.

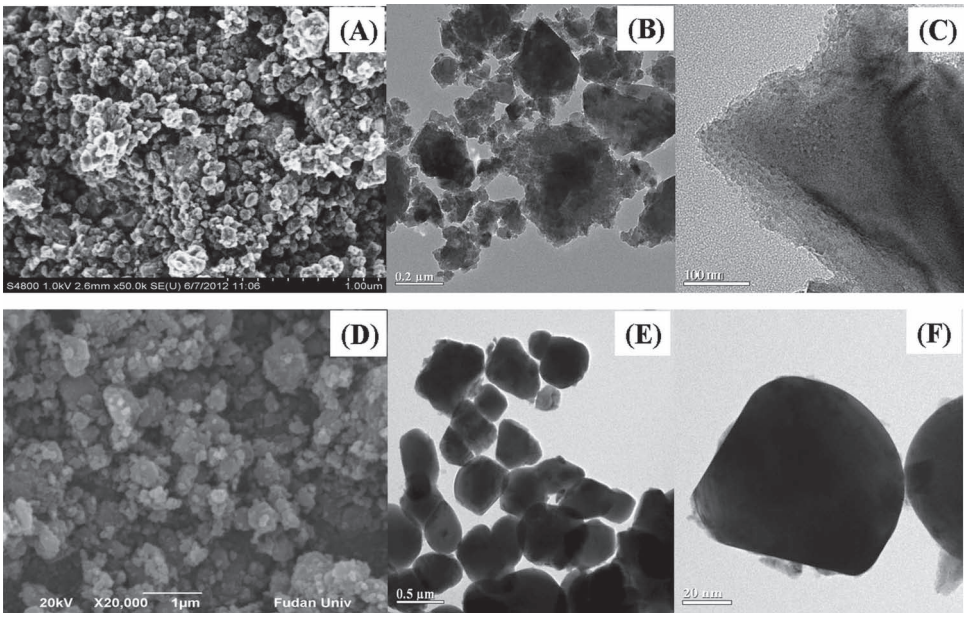

Figure 5. A) SEM image of the sub-micrometer LTO-Q-2 particles and B,C) TEM images of nanoclusters (B) and nanograins (C) for the LTO-Q-2 sample; D) SEM image and E,F) TEM images for the LTO-M sample.

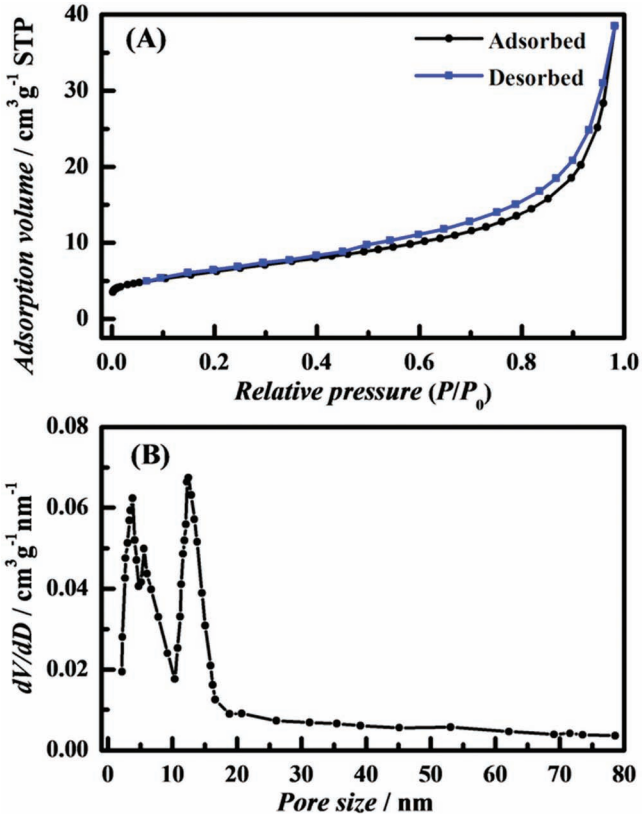

Figure 6. N_2 sorption isotherms (A) and BJH pore size distribution (B) of the LTO-Q-2 sample. The 'STP' (Figure 6A) represents standard temperature and pressure, and 'dV/dD' (Figure 6B) means BJH Differential Pore Size Distribution.

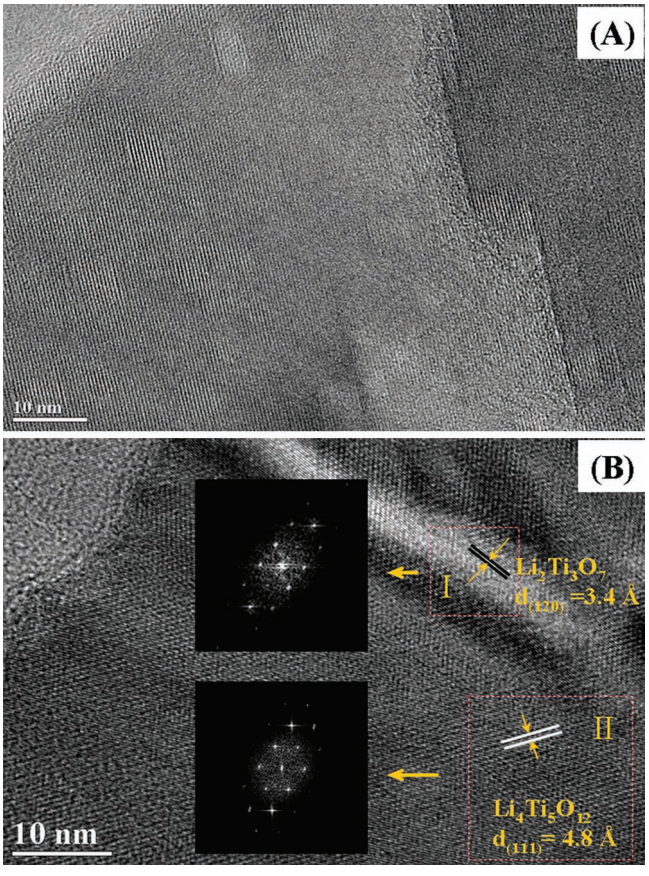

Figure 7. HRTEM images of the LTO-Q-2 sample todetectthe crystalline phase areas (A) and the two co-existing phases of $Li_4Ti_5O_{12}$ and $Li_2Ti_3O_7$ nanocrystals (B), with the corresponding FFT patterns (inset) from the marked regions. The '$d_{(120)}$' and '$d_{(111)}$' represent the lattice spacing of (120) plane of $Li_2Ti_3O_7$ and (111) plane of $Li_4Ti_5O_{12}$, respectively.

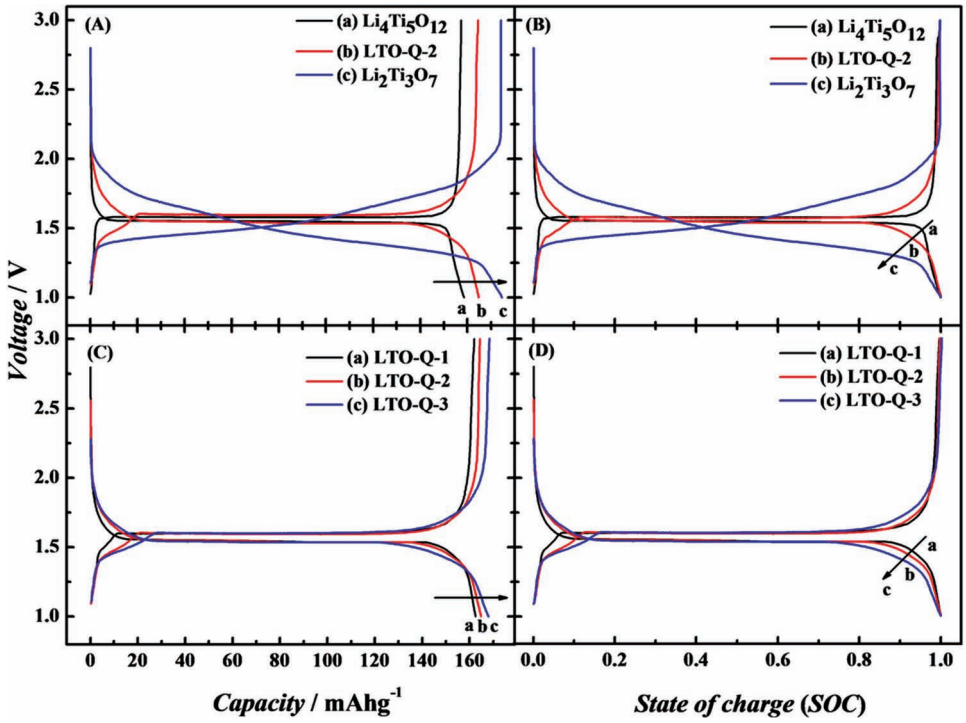

Figure 8. The charge/discharge curves (A) and SOC plots (B) of single-phase $Li_4Ti_5O_{12}$ (a), the LTO-Q-2 sample (b), and single-phase $Li_2Ti_3O_7$ (c); the charge/discharge curves (C) and SOC plots (D) of the LTO-Q-1 (a), LTO-Q-2 (b), and LTO-Q-3 (c) samples. The galvanostatic tests were performed at a current of 32 mA g^{-1} (a C-rate of 0.2 C) in the voltage range of 3 to 1 V.

On one hand, the sloped voltage curve appearing near the end of charge/discharge process is highly desirable to enable a gradual change in voltage, which greatly improves the voltage-based SOC estimation and avoids the overcharging/overdischarging issue caused by a sudden change in voltage. On the other hand, the preservation of flat plateau helps maintain a smooth voltage output. Furthermore, to investigate the influences of the phase composition on charge/discharge profiles of different LTO-Q samples, the charge/discharge curves are given in Figure 8C and D. The total capacity undergoes a slight increase with the addition of $Li_2Ti_3O_7$ content in the binary nanocomposite (Figure 8C), and the capacity in the sloping section near the end of charge/discharge process is also increased gradually (Figure 8D). Thus, the charge/discharge profile can be tailored via a tunable phase composition of the composite in meeting both needs of the smooth voltage output and voltage-based SOC estimation, which is of great significance for practical use of the material in stationary energy storage, where stability and safety weigh over other concerns.[33]

To elucidate the correlation and difference in the charge/discharge curves between the LTO-Q sample and the two compositional phases of $Li_4Ti_5O_{12}$ and $Li_2Ti_3O_7$, the respective differential chronopotentiometric curves (DCCs) converted from the charge/discharge curve is shown in **Figure 9**. For single-phase $Li_4Ti_5O_{12}$, two sharp peaks at 1.572 and 1.556 V are clearly present, corresponding to the charge and discharge plateau in the load curve. In the case of the LTO-Q sample, the potentials for the pair of strongest peaks remain unmodified; however, its shape is somewhat broadened, implying the capacity has a wider coverage of potential. In particular, the ending potential for the cathodic peak shifts from 1.422 to 1.233 V, corresponding to the formation of the sloped region near the end of the discharge curve. Moreover, a small broad anodic peak between 1.421 and 1.522 V is detected, and this is highly consistent with a short sloped stage appearing during the initial charge process. It is also noteworthy that the sharp anodic peak exhibits a broadened phenomenon to a smaller extent than the cathodic peak,

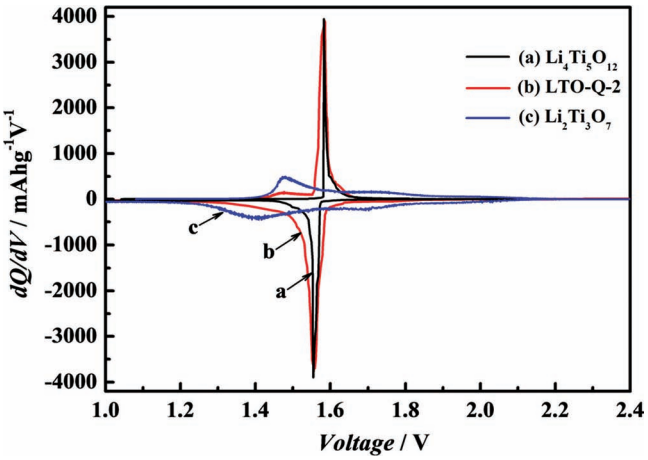

Figure 9. DCCs for single-phase $Li_4Ti_5O_{12}$ (a), the LTO-Q-2 sample (b), and single-phase $Li_2Ti_3O_7$ (c), converted from the charge/discharge curves tested at a current of 8 mA g^{-1} (0.05 C).

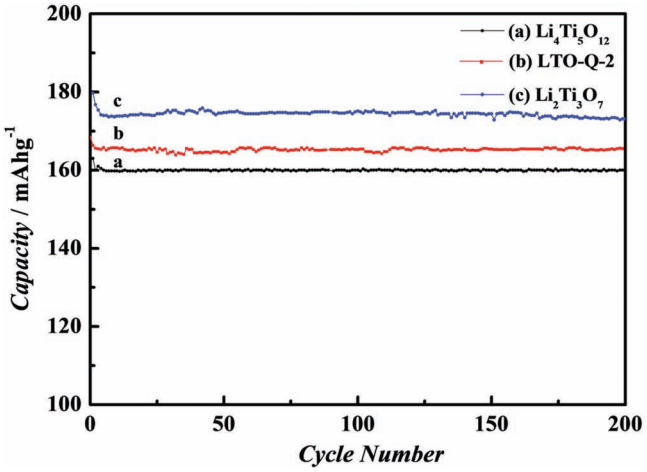

Figure 10. Cycling performance of single-phase $Li_4Ti_5O_{12}$ (a), the LTO-Q-2 sample (b), and single-phase $Li_2Ti_3O_7$ (c) for 200 cycles tested at a current of 32 mA g^{-1} (0.2 C).

contributing to the milder sloped feature at the end of charge process.

The cycling performance of the LTO-Q-2 sample was tested and compared with that of single-phase $Li_4Ti_5O_{12}$ and $Li_2Ti_3O_7$. As illustrated in **Figure 10**, after 200 cycles, the LTO-Q-2 sample demonstrates a desirable cycling stability with a capacity retention of 99.1%, superior to single-phase $Li_2Ti_3O_7$ (98.2%) yet slightly inferior to single-phase $Li_4Ti_5O_{12}$ (99.4%), and the difference between the two single phases could be interpreted in terms of the volume change upon lithium intercalation/extraction.[5,25] In general, it could be concluded that the LTO-Q sample retains the prominent advantage of $Li_4Ti_5O_{12}$ in cyclability, owing to the high crystallinity of the compositional phases and the stability of the hierarchical nanoporous structures.

In order to gain a deep insight into the influence of the hierarchical structure on the electrochemical performance of LTO-Q, the rate capability of the LTO-Q-2 sample was evaluated and compared to a mixer of $Li_4Ti_5O_{12}$ and $Li_2Ti_3O_7$, the LTO-M sample. As **Figure 11**A shows, when the C-rate is progressively increased from 0.2 to 0.5, 1, 2, 5, and 10 C, the discharge capacity of LTO-M declines quickly from the original 166 mA h g^{-1} to 153, 136, 128, 113, and 103 mA h g^{-1}. In contrast, the LTO-Q-2 sample (Figure 11B) demonstrates a slower capacity decay accompanied by a much smaller polarization, such that even at the high C-rate of 10 C, a capacity of 128 mA h g^{-1} is still retained without loss of the flat plateau. To further clarify the difference in rate capability between the two samples, electrochemical impedance spectroscopy (EIS), a promising tool for investigating diffusion issues, was carried out to identify the relationship between the electrochemical performance and electrode kinetics. The Nyquist plots of the LTO-Q and LTO-M electrodes obtained at a certain potential (1.55 V vs Li/Li$^+$) as well as the fitting results using an equivalent circuit are shown in **Figure 12**. It can be seen that each Nyquist plot consists of a high-frequency depressed semicircle between 10^5 and 200 Hz, a Amedium-frequency depressed semicircle between 200 and 0.2 Hz, and a linear Warburg region (W) below 0.2 Hz. The high-frequency semicircle is characteristic of internal resistance,

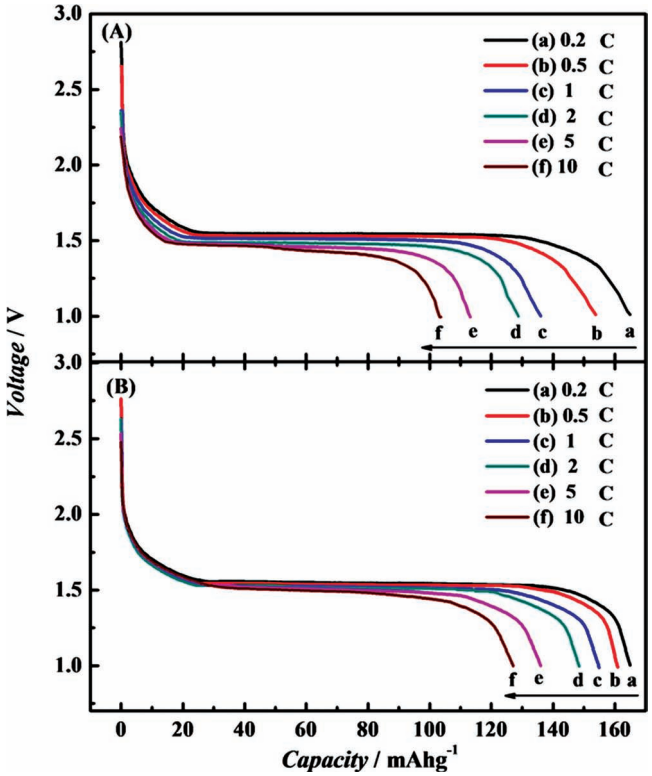

Figure 11. A comparison of the rate capability of the LTO-M (A) and LTO-Q-2 (B)samples under different C-rates (from right to left): 0.2, 0.5, 1, 2, 5, and 10 C, where 1 C corresponds to a current of 160 mA g^{-1}.

including the resistance of the electrode–electrolyte interface, seperator, and electrical contacts, which corresponds to the ohmic resistance (R_Ω) in the equivalent circuit.[34] The internal resistance for LTO-Q ($R_\Omega = 7.8\ \Omega$) is smaller than that for LTO-M ($R_\Omega = 16.5\ \Omega$), indicating a minor interface resistance in the case of LTO-Q, and this should be attributed to the porous feature of the finer nanograins and the decreased contact resistance

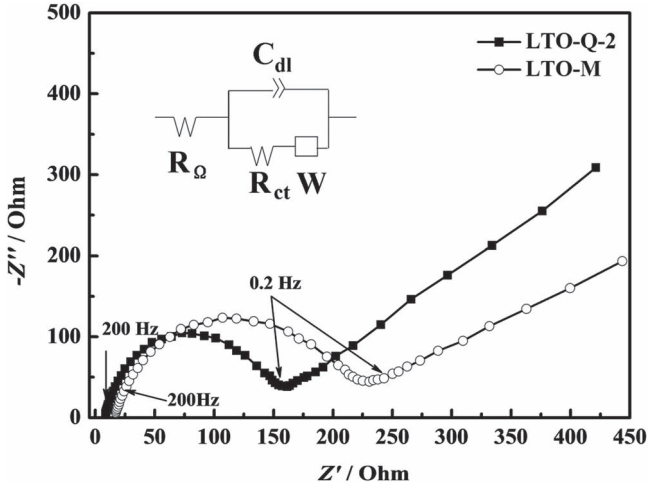

Figure 12. Nyquist plots of the LTO-Q-2 (black rectangles) and LTO-M (white circles) electrodes and fitting results (line) using the equivalent circuit shown in the inset. The Z′ and Z″ represent the real and virtual part of the complex-valued impedance, respectively.

arising from the "nanocomposite" nature. The medium-frequency semicircle is associated with the charge-transfer resistance (R_{ct}) related to lithium-ion interfacial transfer, coupled with a double-layer capacitance (C_{dl}) at the interface. It can be clearly seen that the R_{ct} of LTO-Q is much smaller (R_{ct} = 148.6 Ω) than that of LTO-M (R_{ct} = 219.2 Ω), indicating decreased ionic resistance and enhanced kinetics closely related to a better rate capability. Given the fact that the two samples have a similar particle dimension (≈120 nm) produced by ball milling, it is reasonable to propose the specific hierarchical microstructure as the root cause for the superior high rate performance of the LTO-Q sample. As revealed by the TEM image in Figure 5b and c, the sub-micrometer particle in LTO-Q-2 proves to have a lamellar morphology accumulating in thin layers with nanoporous structure, and this provides much exposure to the electrolyte for facile ionic transport, which cannot occur for the LTO-M sample consisting of dense particles (Figure 5e,f). The process in terms of ion transport is expected to occur in the following way: after the electrolyte enters the particle interior through numerous gateways provided by the exposed thin layers, the numerous nanopores (3–5 nm) are accessible as transport pathways for Li ions to reach the ≈20 nm nanograins, and these grains serve as tiny reaction sites for rapid lithium intercalation and extraction by significantly reducing the diffusion lengths of the Li ions. Most recent reports indicate that the grain boundaries and interfacial areas between the two phases in a composite sample, are favorable for decreasing the charge-transfer resistance via interfacial pseudocapacitive effect, and hence they enhance the rate performance.[32,35]

The optimization in voltage-based SOC estimation of the binary $Li_4Ti_5O_{12}$-$Li_2Ti_3O_7$ nanocomposite anode was further verified in a full cell with a configuration of LTO-Q anode/LFP ($LiFePO_4$) cathode. For comparison, the full cell comprising single-phase $Li_4Ti_5O_{12}$ anode/LFP cathode was also assembled. In the case of the $Li_4Ti_5O_{12}$/LFP full cell (**Figure 13**A), an abrupt voltage rise/drop is inevitable at the end of charge/discharge process, thus leaving a significant safety concern involving overcharging/overdischarging. In contrast, the situation is significantly improved in the case of the fuel cell with the LTO-Q anode/LFP cathode system (Figure 13B). An extended sloped curve is observed within the range of 1.9–2.5 V during charge and within 1.8–1.0 V during discharge; this provides an effective indicator for signalling the real-time SOC, and it precisely predicts the end of the charge/discharge process allowing avoidance of overcharging/overdischarging.

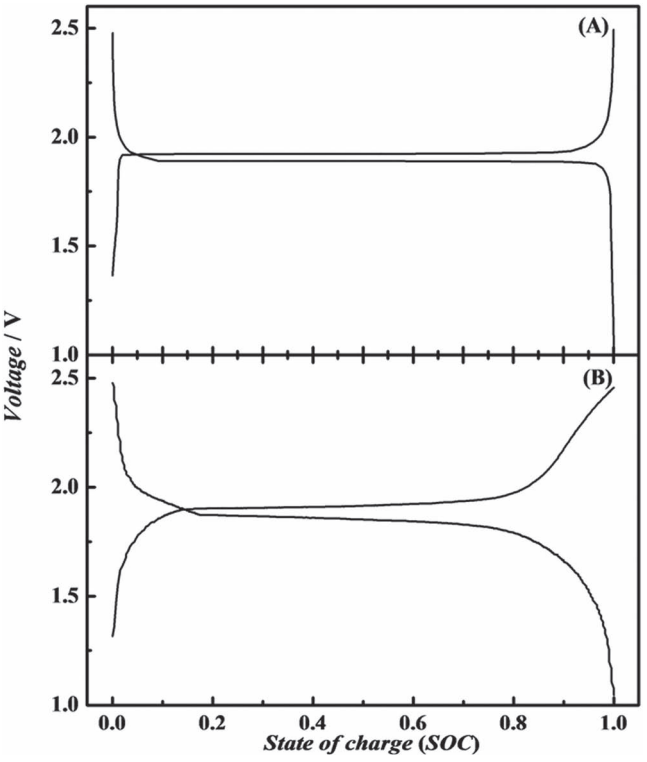

Figure 13. The typical charge/discharge curves of the $Li_4Ti_5O_{12}$/$LiFePO_4$ full cell (A) and theLTO-Q-2/$LiFePO_4$ full cell (B) tested at a rate of 0.5 C (80 mA g^{-1}).

3. Conclusion

We developed a facile way to prepare a highly crystalline binary $Li_4Ti_5O_{12}$-$Li_2Ti_3O_7$ nanocomposite using a solid-state method involving quench assistance by liquid N_2. By controlling the temperature and cooling rate, a lamellar morphology consisting of interconnected nanograins of ≈20 nm size with a hierarchical nanoporous structure is produced within the composite; this is confirmed by TEM and pore size distribution analysis. Compared with the simple mixture of $Li_4Ti_5O_{12}$ and $Li_2Ti_3O_7$, the dual-phase nanocomposite exhibits a much better rate capability, maintaining a capacity of 128 mA h g^{-1} even at the high C-rate0 of 10 C. Most importantly, the significant difficulty in the voltage-based SOC estimation of the $Li_4Ti_5O_{12}$ anode due to the sudden voltage rise/drop near the end of charge/discharge state is overcome by introducing the $Li_2Ti_3O_7$ phase. Moreover, the SOC range for the flat and sloped voltage profile can be tuned by altering the $Li_4Ti_5O_{12}$:$Li_2Ti_3O_7$ ratio in the composite, such that it meets the both requirements of a smooth voltage output and prevention of overcharging/overdischarging.

4. Experimental Section

Synthesis: The binary $Li_4Ti_5O_{12}$-$Li_2Ti_3O_7$ nanocomposites (designated as LTO-Q), with various weight ratios of $Li_4Ti_5O_{12}$:$Li_2Ti_3O_7$ of 85:15, 75:25, and 65:35, were prepared by a quench-assisted solid-state method as follows. Stoichiometric TiO_2 (AR, Shanghai Chemical Agents Co. Ltd., China) and Li_2CO_3 (AR, Shanghai Chemical Agents Co. Ltd., China) were mixed well according to the targeted $Li_4Ti_5O_{12}$:$Li_2Ti_3O_7$ ratios (e.g., in the case of the 85:15 nanocomposite, the weight ratio of Li_2CO_3:TiO_2 was 9:25) by ball-milling for 1 h, and then the mixture was annealed at 970 °C for 14 h under air in a muffle furnace, followed by quenching in liquid N_2. The as-prepared samples with the weight ratios of 85:15, 75:25, and 65:35 for $Li_4Ti_5O_{12}$:$Li_2Ti_3O_7$ were designated as LTO-Q-1, LTO-Q-2, and LTO-Q-3, respectively. For comparison, another composite sample in the ratio of 75:25 was prepared under similar preparation conditions (970 °C, 14 h), except that natural cooling was used in place of quenching; the resulting sample was designated as LTO-NC. Single-phase $Li_4Ti_5O_{12}$ and single-phase $Li_2Ti_3O_7$ were prepared using a conventional solid-state method by annealing at 800 and 1050 °C,

respectively, under air for 14 h. Additionally, a mixer of $Li_4Ti_5O_{12}$ and $Li_2Ti_3O_7$ (designated as LTO-M) was obtained by mechanically mixing the two single phases at a $Li_4Ti_5O_{12}$:$Li_2Ti_3O_7$ weight ratio of 75:25. In order to compare their electrochemical properties under similar particle sizes, all above samples (LTO-Q, LTO-NC, and LTO-M) were ball-milled in a high-energy planetary monomill (Fritsch Pulverisette 6) at the rate of 250 rpm for 3 h, and the resulting powders were sifted to approximately 300 mesh. The $LiFePO_4$ (LFP) material used in this work was a commercial product (Golden Horse Energy Co. Ltd., China).

Characterization: The phase purity of all samples were characterized by powder XRD (Bruker D2 Phaser Table-top Diffractometer) using Cu-Kα radiation at 30 kV and 10 mA between 10 and 90° (2θ), with a step size of 0.02° (2θ) and step time of 0.2 s. The phase composition of different LTO-Q samples were further identified using Rietveld refinement (Bruker 2009, Total Pattern Analysis Solution Software V4.2) using the XRD data obtained under a longer step time of 4 s.

The morphologies of the different samples were characterized using SEM (Hitachi FE-SEM S-4800) and TEM (Joel JEM-2100F). Nitrogen sorption isotherms were measured at 77 K after samples were degassed at 300 °C for at least 3 h (Quadrasorb SI Automated Surface Area and Pore Size Analyzer). The specific surface area and pore size distribution were derived using the multipoint BET method and the BJH model, respectively.

Electrochemical Tests: Each working electrode of the different samples was prepared by mixing 80 wt% active material, 10 wt% carbon black, and 10 wt% polyvinyl difluoride (PVDF) dispersed in 1-methyl-2-pyrrolidinone (NMP). Subsequently, the slurry was cast uniformly on aluminum foil. The electrode film was vacuum-dried at 100 °C for 1 h to remove the solvent before roll-pressing. The electrode film was then punched into discs with diameters of 12 mm and vacuum-dried at 80 °C for 12 h. The typical mass load of active material was controlled to be about 6 mg cm^{-2}.

Galvanostatic charge/discharge tests were carried out in CR2016-type coin cells, and the cells were assembled in a glove-box filled with Ar atmosphere. For the half-cell test, metallic lithium was used as the anode, with lithium intercalation into the LTO electrode being referred to as "discharge" and extraction as "charge". For the full cell, $LiFePO_4$ (LFP) was used as the cathode, and the LFP electrode film was prepared by a similar route as described above, with lithium insertion into the LTO electrode being referred to as "charge" and extraction as "discharge". The electrolyte solution was 1 M $LiPF_6$-ethylene carbonate (EC)/diethyl carbonate (DMC)/ethyl methyl carbonate (EMC) (1:1:1 by volume). The galvanostatic electrochemical test was evaluated under an automatic battery testing system (LAND CT2001A model).

EIS tests were carried out using a T-shaped three-electrode cell, which was assembled using the LTO-Q or LTO-M electrode as the working electrode and lithium metal as both the counter and reference electrodes, and performed in three steps. First, the cell was discharged to a certain potential (1.55 V vs Li/Li^+,110 mA h g^{-1}); second, the cell was maintained for several hours for equilibration. Finally, an EIS test was conducted at a certain potential (Solartron Instrument Model 1287 electrochemical interface and 1255B frequency response analyzer). The frequency limits were typically set within 10^5–10^{-2} Hz.

Supporting Information

Supporting Information is available from the Wiley Online Library or from the author.

Acknowledgements

This work was partially supported by the State Key Basic Research Program of PRC (2011CB935903), National Natural Science Foundation of China (20925312) and the Shanghai Science & Technology Committee (10JC1401500, 08DZ2270500).

Received: June 26, 2012
Revised: August 7, 2012
Published online: September 11, 2012

[1] P. G. Bruce, B. Scrosti, J. M. Tarascon, *Angew. Chem. Int. Ed.* **2008**, *47*, 2930.
[2] M. Inaba, *Electrochemistry* **2010**, *78*, 318.
[3] J. Xiao, X. L. Chen, P. V. Sushko, M. L. Sushko, L. Kovarik, J. J. Feng, Z. Q. Deng, J. M. Zheng, G. L. Graff, Z. M. Nie, D. Choi, J. Liu, J. G. Zhang, M. S. Whittingham, *Adv. Mater.* **2012**, *24*, 2109.
[4] A. N. Jansen, A. J. Kahaian, K. D. Kepler, P. A. Nelson, K. Amine, D. W. Dees, D. R. Vissers, M. M. Thackeray, *J. Power Sources* **1999**, *902*, 81.
[5] K. Nakahara, R. Nakajima, T. Matsushima, H. Majima, *J. Power Sources* **2003**, *117*, 131.
[6] C. H. Jiang, Y. Zhou, I. Honma, T. Kudo, H. S. Zhou, *J. Power Sources* **2007**, *166*, 514.
[7] G. N. Zhu, C. X. Wang, Y. Y. Xia, *J. Electrochem. Soc.* **2011**, *158*, A102.
[8] C. H. Jiang, M. Ichihara, I. Honma, H. S. Zhou, *Electrochim. Acta* **2007**, *52*, 6470.
[9] L. Zhao, Y. S. Hu, H. Li, Z. X. Wang, L. Q. Chen, *Adv. Mater.* **2011**, *23*, 1385.
[10] L. Cheng, H. J. Liu, J. J. Zhang, H. M. Xiong, Y. Y. Xia, *J. Electrochem. Soc.* **2006**, *153*, A1472.
[11] H. M. Xie, R. S. Wang, J. R. Ying, L. Y. Zhang, A. F. Jalbout, H. Y. Yu, G. L. Yang, X. M. Pan, Z. M. Su, *Adv. Mater.* **2006**, *18*, 2609.
[12] E. Kang, Y. S. Jung, G. H. Kim, J. Y. Chun, U. Wiesner, A. C. Dillon, J. K. Kim, J. W. Lee, *Adv. Funct. Mater.* **2011**, *21*, 4349.
[13] L. Cheng, J. Yan, G. N. Zhu, J. Y. Luo, C. X. Wang, Y. Y. Xia, *J. Mater. Chem.* **2010**, *20*, 595.
[14] G. N. Zhu, H. J. Liu, J. H. Zhuang, C. X. Wang, Y. G. Wang, Y. Y. Xia, *Energy Environ. Sci.* **2011**, *4*, 4016.
[15] H. W. Lu, W. Zeng, Y. S. Li, Z. W. Fu, *J. Power Sources* **2007**, *164*, 874.
[16] E. M. Sorensen, S. J. Barry, H. K. Jung, J. R. Rondinelli, J. T. Vaughey, K. R. Poeppelmeier, *Chem. Mater.* **2006**, *18*, 482.
[17] B. Kang, G. Ceder, *Nature* **2009**, *190*, 458.
[18] A. Yamada, H. Koizumi, S. I. Nishimura, N. Sonoyama, R. Kanno, M. Yonemura, T. Nakamura, Y. Kobayashi, *Nat. Mater.* **2006**, *5*, 357.
[19] J. Wang, M. W. Verbrugge, P. Liu, *J. Electrochem. Soc.* **2010**, *157*, A185.
[20] N. Meethong, H. Y. S. Huang, W. C. Carter, Y. M. Chiang, *Electrochem. Solid-State Lett.* **2007**, *10*, A134.
[21] N. Meethong, H. Y. S. Huang, S. A. Speakman, W. C. Carter, Y. M. Chiang, *Adv. Funct. Mater.* **2007**, *17*, 1115.
[22] A. Jaiswal, C. R. Horne, O. Chang, W. Zhang, W. Kong, E. Wang, T. Chern, M. M. Doeff, *J. Electrochem. Soc.* **2009**, *156*, A1041.
[23] J. Gao, J. R. Ying, C. Y. Jiang, C. R. Wan, *J. Inorg. Mater.* **2009**, *24*, 139.
[24] W. Cho, T. Kashiwagi, W. Ra, M. Nakayama, M. Wakihara, Y. Kobayashi, H. Miyashiro, *Electrochim. Acta* **2009**, *54*, 1842.
[25] M. E. Arroyo de Dompablo, E. Moran, A. Varez, F. Garcia-Alvarado, *Mater. Res. Bull.* **1997**, *32*, 993.
[26] M. E. Arroyo de Dompable, A. Varez, F. Garcia-Alvarado, *J. Solid State Chem.* **2000**, *153*, 132.
[27] F. Garcia-Alvarado, M. E. Arroyo de Dompablo, E. Moran, M. T. Gutierrez, A. Kuhn, A. Varez, *J. Power Sources* **1999**, *85*, 81.
[28] J. A. Mergos, C. T. Dervos, *Mater. Charact.* **2009**, 848.
[29] G. Izquierdo, A. R.West, *Mater. Res. Bull.* **1980**, *15*, 1655.
[30] K. Amine, I. Belharouak, Z. H. Chen, T. Tran, H. Yumoto, N. Ota, S. T. Myung, Y. K. Sun, *Adv. Mater.* **2010**, *22*, 3052.
[31] L. F. Shen, C. Z. Yuan, H. J. Luo, X. G. Zhang, K. Xua, Y. Y. Xia, *J. Mater. Chem.* **2010**, *20*, 6998.
[32] M. M. Rahman, J. Z. Wang, M. F. Hassan, D. Wexler, H. K. Liu, *Adv. Energy Mater.* **2011**, *1*, 212.
[33] T. Xu, W. Wang, M. L. Gordin, D. H. Wang, D. Choi, *JOM* **2010**, *62*, 24.
[34] J. Wolfenstine, U. Lee, J. L. Allen, *J. Power Sources* **2006**, *154*, 287.
[35] J. Jamnika, J. Maier, *Phys. Chem. Chem. Phys.* **2003**, *5*, 5215.